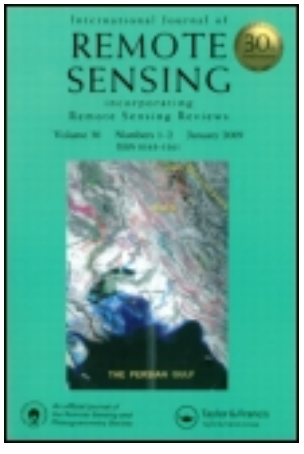

International Journal of Remote Sensing

Publication details, including instructions for authors and subscription information:
http://www.tandfonline.com/loi/tres20

Changes in snow and glacier cover in an arid watershed of the western Kunlun Mountains using multisource remote-sensing data

Jiangfeng She[a], Yufang Zhang[a], Xingong Li[bc] & Yaning Chen[b]

[a] Department of Geographical Information Science, Nanjing University, Nanjing, China

[b] Xinjiang Institute of Ecology and Geography, Chinese Academy of Sciences, Wulumuqi, China

[c] Department of Geography, University of Kansas, Lawrence, KS, USA

Published online: 24 Dec 2013.

To cite this article: Jiangfeng She, Yufang Zhang, Xingong Li & Yaning Chen (2014) Changes in snow and glacier cover in an arid watershed of the western Kunlun Mountains using multisource remote-sensing data, International Journal of Remote Sensing, 35:1, 234-252, DOI: 10.1080/01431161.2013.866296

To link to this article: http://dx.doi.org/10.1080/01431161.2013.866296

International Journal of Remote Sensing, 2014
Vol. 35, No. 1, 234–252, http://dx.doi.org/10.1080/01431161.2013.866296

Taylor & Francis
Taylor & Francis Group

Changes in snow and glacier cover in an arid watershed of the western Kunlun Mountains using multisource remote-sensing data

Jiangfeng She[a], Yufang Zhang[a], Xingong Li[b,c]*, and Yaning Chen[b]

[a]*Department of Geographical Information Science, Nanjing University, Nanjing, China;* [b]*Xinjiang Institute of Ecology and Geography, Chinese Academy of Sciences, Wulumuqi, China;* [c]*Department of Geography, University of Kansas, Lawrence, KS, USA*

(*Received 11 June 2013; accepted 24 October 2013*)

Snow and glaciers in the mountain watersheds of the Tarim River basin in western China provide the primary water resources to cover the needs of downstream oases. Remote sensing provides a practical approach to monitoring the change in snow and glacier cover in those mountain watersheds. This study investigated the change in snow and glacier cover in one such mountain watershed using multisource remote-sensing data, including the Moderate Resolution Imaging Spectroradiometer (MODIS), Landsat (Multispectral Scanner (MSS), Thematic Mapper (TM), and Enhanced Thematic Mapper Plus (ETM+)), Corona, and Google Earth™ imagery. With 10 years' daily MODIS snow-cover data from 2002 to 2012, we used two de-cloud methods before calculating daily snow-cover percentage (SCP), annual snow-cover frequency (SCF), and annual minimum snow-cover percentage (AMSCP) for the watershed. Mann–Kendall analysis showed no significant trend in any of those snow-cover characterizations. With a total of 22 Landsat images from 1967 to 2011, we used band ratio and supervised classification methods for snow classification for Landsat TM/ETM+ images and MSS images, respectively. The Landsat snow-cover data were divided into two periods (1976–2002 and 2004–2011). Statistical tests indicated no significant difference in either the variance or mean of SCPs between the two periods. Three glaciers were identified from Landsat images of 1998 and 2011, and their total area increased by 12.6%. In addition, three rock glaciers were also identified on both the Corona image of 1968 and the Google high-resolution image of 2007, and their area increased by 2.5%. Overall, based on multisource remote-sensing data sets, our study found no evidence of significant changes in snow and glacier cover in the watershed.

1. Introduction

Seasonal snow packs and glaciers in more than 50% of mountain areas globally have an essential or supportive role for downstream water resources (Viviroli et al. 2007). Snow-cover extent in the Northern Hemisphere has been declining since the 1970s and is coincident with hemispheric warming (Dery and Ross 2007; Flanner et al. 2011). Global annual glacier mass-balance data indicate a marked glacier loss in the Northern Hemisphere (Ohmura 2006; Zemp, Hoelzle, and Haeberli 2009). A recent study on glacier contribution to sea level rise also indicates a global glacier mass loss, though this loss is less negative than local measurements (Gardner et al. 2013). Most Himalayan glaciers are losing mass at rates similar to glaciers elsewhere, except that there is evidence of stability or mass gain in the Karakoram (Bolch et al. 2012). Gardner et al. (2013) also found that

*Corresponding author. Email: lixi@ku.edu

the glaciers of high-mountain Asia showed a loss of mass but with a spatially heterogeneous pattern within the region.

Change in snow and glacier cover in those mountainous areas is likely to disrupt downstream water resources, especially in areas where mountain water cannot compensate for large lowland deficits (Viviroli et al. 2007). Immerzeel, van Beek, and Bierkens (2012) analysed the relevance of snow and glacier melt in basin hydrology and climate change impacts on downstream water supply and food security in five Asian watersheds and concluded that Asian water towers are threatened but the impacts differ substantially and cannot be generalized. Bolch et al. (2012) also indicated a heterogeneous impact in the region where glacier meltwater is a major source of stream flow in the Karakoram and northwestern Himalaya with little summer precipitation but is less important in monsoon-dominated regions with abundant summer precipitation. While glacier contribution is negligible in the lowlands of river basins governed by monsoon climates, Kaser, Grosshauser, and Marzeion (2010) found that glacier contribution is highest where rivers enter seasonally arid regions, such as the Tarim River basin.

Our study watershed is located in the western Kunlun Mountains and is at the southern edge of the Tarim River basin, which is the largest continental river basin in the world and is surrounded by mountain watersheds dominated by snow and glacier cover. Within the Tarim River basin, mountain-fed rivers are the primary water resources to cover the needs of the oases scattered along its waterway into the Taklimakan Desert for public supply, agriculture irrigation, hydropower, and other uses (Li and Williams 2008). Snow and glaciers in these mountain watersheds play an important role in forming the flow regime, which depends on snow and glacier melt rather than the timing of precipitation, and these are sensitive to changes in climatic conditions. It has been reported that, in recent decades, most glaciers in this area have shown wide and continuous recession, presumably driven by increasing temperatures (Yao et al. 2004; Ye et al. 2006; Shangguan et al. 2006; Shangguan 2009).

Remote sensing provides a practical, if not the only, approach to monitoring snow and glacier change in these mountain watersheds, due to their hostile environment and inaccessibility. The objective of this study was to investigate changes in snow and glaciers in one of the mountain watersheds in the Tarim River basin using multiple remote-sensing data sources, including the Moderate Resolution Imaging Spectroradiometer (MODIS), Landsat (Multispectral Scanner (MSS), Thematic Mapper (TM), and Enhanced Thematic Mapper Plus (ETM+)), and declassified Corona imagery. We examined the trend of annual minimum snow-cover percentage (SCP) and the trend of snow-cover frequency (SCF) using 10 years' daily MODIS snow-cover data. We tested the differences in variance and mean of SCP derived from Landsat images spanning 1976 to 2011. We also investigated the change in extent of three glaciers from Landsat images of 1998 and 2011 and of three rock glaciers from high-resolution images of 1968 and 2007. Our study demonstrated the usefulness and limitations of remote-sensing data of various spatial and temporal resolutions and time spans in the study of snow and glacier changes in mountain watersheds.

2. Study area and data

2.1. Study area

The Tizinafu watershed (Figure 1) covers an area of 5518 km^2, with elevation ranging between 1575 and 6234 m and a mean of 3605 m. It is a typical mountain watershed in the Kunlun Mountains where snow and glacier melt accounts for most of the river flow at

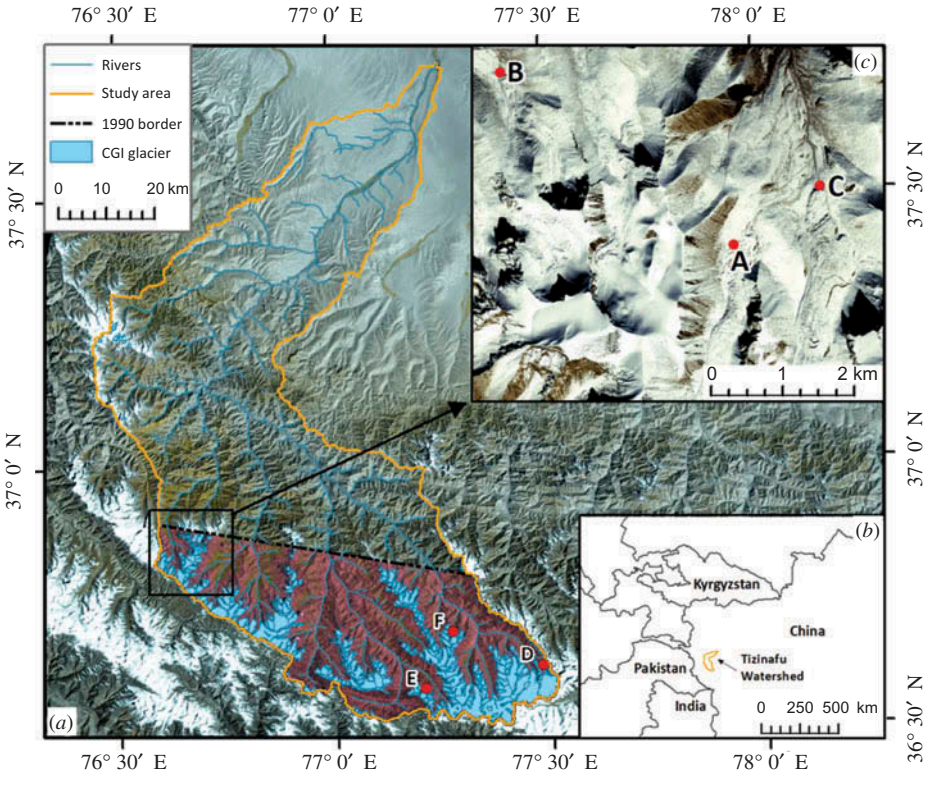

Figure 1. (*a*) The Tizinafu mountain watershed. The solid black rectangle is the area where three rock glaciers were examined using Corona and Google Earth imagery. The dashed black line and area shaded dark red indicate the intersection between the 29 June 1990 Landsat TM scene at 148/35 and the watershed. Change analysis using Landsat images was performed only in this portion of the watershed. D, E, and F denote glaciers identified from the Landsat images; (*b*) location of the watershed in western China; (*c*) locations of three rock glaciers A, B, and C in the watershed.

the watershed outlet. The primary land cover in the watershed is bare ground (51%), open shrubland (35%), grassland (9%), and wood/grassland (5%) (Li and Williams 2008). According to the Chinese Glacier Inventory (CGI) (Shi, Liu, and Kang 2010), the glaciers in the Tizinafu basin cover an area of 351 km^2 (i.e. 6.3% of the watershed). Average annual precipitation at the watershed outlet is 120 mm and average minimum and maximum temperatures are –12°C and 29°C, respectively (Li and Williams 2008). Landsat scene 148/35 in the WRS-2 worldwide reference system covers the southernmost quarter of the watershed where the majority of snow and glaciers are located. Among all Landsat scenes available at 148/35, the Landsat TM image of 29 June 1990 has the least coverage in the watershed. The dashed black line in Figure 1(*a*) indicates the northern boundary of the 1990 Landsat TM scene. The intersection of the 1990 Landsat TM scene and the watershed, which is the common area covered by all available Landsat images, was therefore used for change analysis. Glaciers D, E, and F in Figure 1(*a*) were identified from the Landsat images of 1988 and 2011 and the change in their extent was investigated. The solid black rectangle in Figure 1(*a*) indicates the area within which three individual rock glaciers (A, B, and C in Figure 1(*c*)) were examined using Corona and high-resolution Google Earth^{TM} imagery.

2.2. MODIS snow-cover data

MODIS is one of the instruments on the Terra spacecraft which was launched in December 1999 and began producing data in February 2000. A second MODIS instrument on the Aqua spacecraft was launched in May 2002, and started collecting data in July 2002. MODIS is a 36-channel instrument from which standard snow-cover products are produced in an automatic production environment (MODIS 2010). The snow-cover products used in this study are version 5 of the standard MODIS global daily snow-cover product MOD10A1 (Terra) and MYD10A1 (Aqua) at a spatial resolution of 500 m, covering 10 hydrological years from 1 October 2002 to 30 September 2012. The daily products provide snow cover, snow albedo, and fractional snow cover, though this study used only snow-cover data. Daily snow-cover data MOD10A1 and MYD10A1 were downloaded from NASA FTP servers n4ftl01u.ecs.nasa.gov/SAN/MOST and n4ftl01u.ecs.nasa.gov/SAN/MOSA, respectively.

2.3. Landsat images

Landsat MSS, TM, and ETM+ images were downloaded from the United States Geological Survey (USGS) website (http://glovis.usgs.gov/index.shtml) and they were chosen based on two criteria: (1) acquisition date between June and September to minimize interference from seasonal snow and (2) no or low cloud cover, as it is impossible to extract snow and glaciers underneath cloud cover. There are 22 Landsat images (3 MSS, 6 TM, and 13 ETM+) available from the USGS spanning 1976 to 2011, and these were used in our study.

2.4. Corona images

Corona is the US first programme of intelligence satellites that operated from 1959 to 1972. Images acquired from Corona camera systems were declassified in 1996 and became available in digital format in 2003 (Dashora, Lohani, and Malik 2007; Gheyle et al. 2011). Later generations of the Corona series, such as KH-4A and KH-4B (KH denotes keyhole), had both forward and aft panoramic cameras which enabled stereo capability. Corona images are of great value in examining long-term glacier changes because they recorded the surface condition existing about 50 years ago at relatively high spatial resolution, especially in those areas where historic aerial photography is difficult to obtain (Bhambri et al. 2011; Bhambri, Bolch, and Chaujar 2011). On the other hand, distortions from panoramic photography and the lack of ephemeris parameters of camera systems have hindered the extensive usage of Corona images. Two Corona images (DS1104-2185DA105 and DS1104-2185DF100) were obtained from USGS in digital format scanned at 3600 dpi. The two images were taken by the KH-4B camera system on 19 August 1968, with the best ground resolution of about 1.8 m at nadir. In addition, the panchromatic band (with a spatial resolution of 15 m) of Landsat ETM+ scene 148/35 on 18 May 2001, downloaded from the Global Landcover Facility (www.landcover.org), was also used to rectify the Corona images.

3. Methods

3.1. MODIS snow-cover analysis

One of the major limits of using MODIS daily snow-cover data is the high portion of cloud cover in mountain areas. Since satellites Terra and Aqua pass the equator with a 3 hour difference (at 10:30 am for Terra and 1:30 pm for Aqua) and clouds move in most cases, a combination of Terra and Aqua snow-cover products is more likely to successfully detect snow cover than can either Terra or Aqua alone (Wang and Xie 2009). We

developed a similar algorithm that combined daily MODIS snow-cover products MOD10A1 and MYD10A1 and generated a more cloud-free daily snow-cover product (MOYD10A1 hereafter). Our algorithm first reclassified Terra's MOD10A1 and Auqa's MYD10A1 data into four general categories (snow, land, cloud, and missing). When combining the two reclassified data, a cell would be categorized as snow when it is snow on *either* the Terra or Aqua image and as cloud only when it is cloud on both Terra and Aqua images. Except for snow, Terra classes were used as the primary data source whenever there was inconsistency between Terra and Aqua classes. To further reduce cloud obstruction, we processed the MOYD10A1 data by assigning to one cell, in the case of cloud cover, the land-cover class of the most recent clear observation within a 7 day window, assuming that land-cover changes are not very marked within the temporal window (Parajka and Bloschl 2008).

We then calculated daily SCP and SCF within a hydrological year (1 October to 30 September) to examine their spatial and temporal trends. Daily SCP within a watershed was calculated as the ratio between the number of cells in the watershed covered by snow and that not obstructed by clouds. This gives the best SCP estimate when clouds occur randomly within a watershed. Similarly, the SCF of a cell during the period of one hydrological year was calculated as the ratio between the number of days with snow covered and that not obstructed by clouds in the cell. This approach gives the best SCF estimate when clouds occur equally on snow and no-snow days.

Annual minimum snow-cover percentage (AMSCP hereafter), is a good indicator of climate change, as increasing temperature is likely to reduce the minimum (or perennial) snow cover within a watershed. This can be calculated by either finding the minimum daily SCP values within a hydrological year or calculating the percentage of cells within a watershed with SCF of 100% within 1 year (i.e. cells that are always covered by snow when not obscured by clouds). The Mann–Kendall trend test, a nonparametric test for monotonic trends (Helsel and Hirsch 2002), was used to analyse trends.

3.2. *Snow classification and glacier delineation from Landsat images*

The normalized difference snow index (NDSI) is a widely used approach in identifying and mapping snow cover (Hall, Riggs, and Salomonson 1995; Hall et al. 1998). For Landsat TM data, NDSI is calculated as NDSI = (band2 – band5)/(band2 + band5). The direct ratio between a visible band and mid-infrared band is also a method commonly used to extract snow and ice cover extent from Landsat images. Both NDSI and simple band ratio methods are effective for identification of snow cover and for separating snow cover from clouds (Dozier 1989; Hall, Riggs, and Salomonson 1995; Hall, Riggs, and Salomonson 2001; Paul et al. 2002). For Landsat TM data, two simple band ratios (band3/band5 and band4/band5) were widely used as these have been proved successful in delineating snow cover in previous studies (Hall et al. 1987; Williams, Hall, and Benson 1991; Paul et al. 2002; Bolch and Kamp 2006; Frey, Paul, and Strozzi 2012; Andreassen et al. 2008).

The Landsat TM image of 10 August 2011 was used to compare snow cover derived from band ratios and NDSI. NDSI values greater than or equal to 0.4 were generally found to represent snow cover well (Hall, Riggs, and Salomonson 1995), and this value was chosen as the threshold in our comparison. Simple band ratio threshold values were determined through visual comparison. With ratio thresholds varying from 1.0 to 3.0, snow cover extent from band ratio images varied little and were visually indistinguishable. Figure 2(*a*) shows the common area of snow cover extracted from NDSI and two simple band ratio images (band3/band5 and band4/band5), both using a ratio threshold value of 2.0.

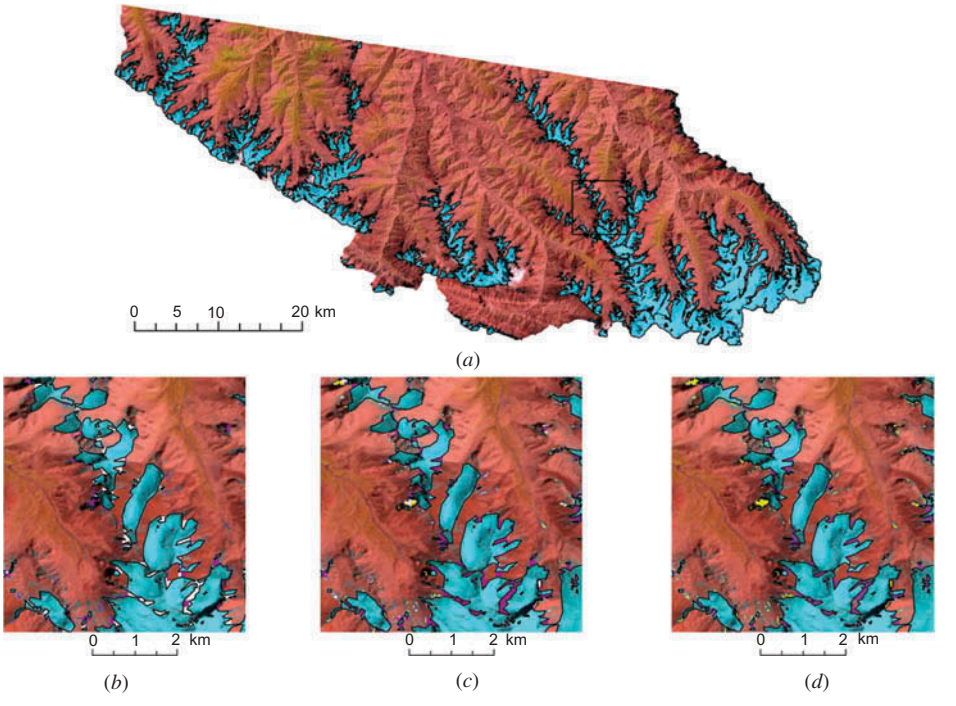

Figure 2. (*a*) A pseudo-colour Landsat image of 10 August 2011 for the southern portion of the Tizinafu watershed in Figure 1(*a*) overlaid with the common area of snow cover extracted from simple band ratios of band3/band5, band4/band5, and NDSI. A detailed view and pairwise comparison of snow cover extracted by these methods inside the black rectangle are shown in (*b*), where purple, yellow, and white are the areas unique to ratios band3/band5 and band4/band5, and those common to both ratio methods, respectively; in (*c*), where purple, yellow, and white are the areas unique to ratios band3/band5 and NDSI, and common to both methods, respectively; and in (*d*), where purple, yellow, and white are the areas unique to ratios band4/band5 and NDSI, and common to both methods, respectively. Black outlines in (*b*) to (*d*) are the intersections of the three methods.

Little difference was noted among these, except that snow-cover area from the NDSI image was marginally smaller than that from the band ratio images. Figures 2(*b–d*) show detailed views and comparisons of a portion of snow cover extracted from band ratios and NDSI. Little difference was observed between the two simple ratio methods. No waterbody was misclassified by either method, as the ratios for waterbodies are somewhat lower than the thresholds used for snow. Both simple band ratios and NDSI classified snow under shadow correctly, as these ratio-based methods largely removed the effect of shadow. Based on these analyses, snow cover on Landsat images was extracted using the simple band ratio of band4/band5 with a threshold value of 2.0.

A problem with the simple band ratio method when using Landsat MSS is the lack of a middle infrared band (band 5 in TM and ETM+) in Landsat MSS. Because of this, a supervised classification was also used to classify three Landsat MSS images from the 1970s. To confirm the comparability of snow cover derived from supervised classification and the band ratio method, we applied both methods to the Landsat TM image of 10 August 2011 for verification. Following Naz, Bowling, and Crawford (Forthcoming), five classes of training samples (no-snow land, water, snow under shadow, snow-covered ice, and snow-free ice) were used in our supervised classification (Figure 3(*a*)). Following

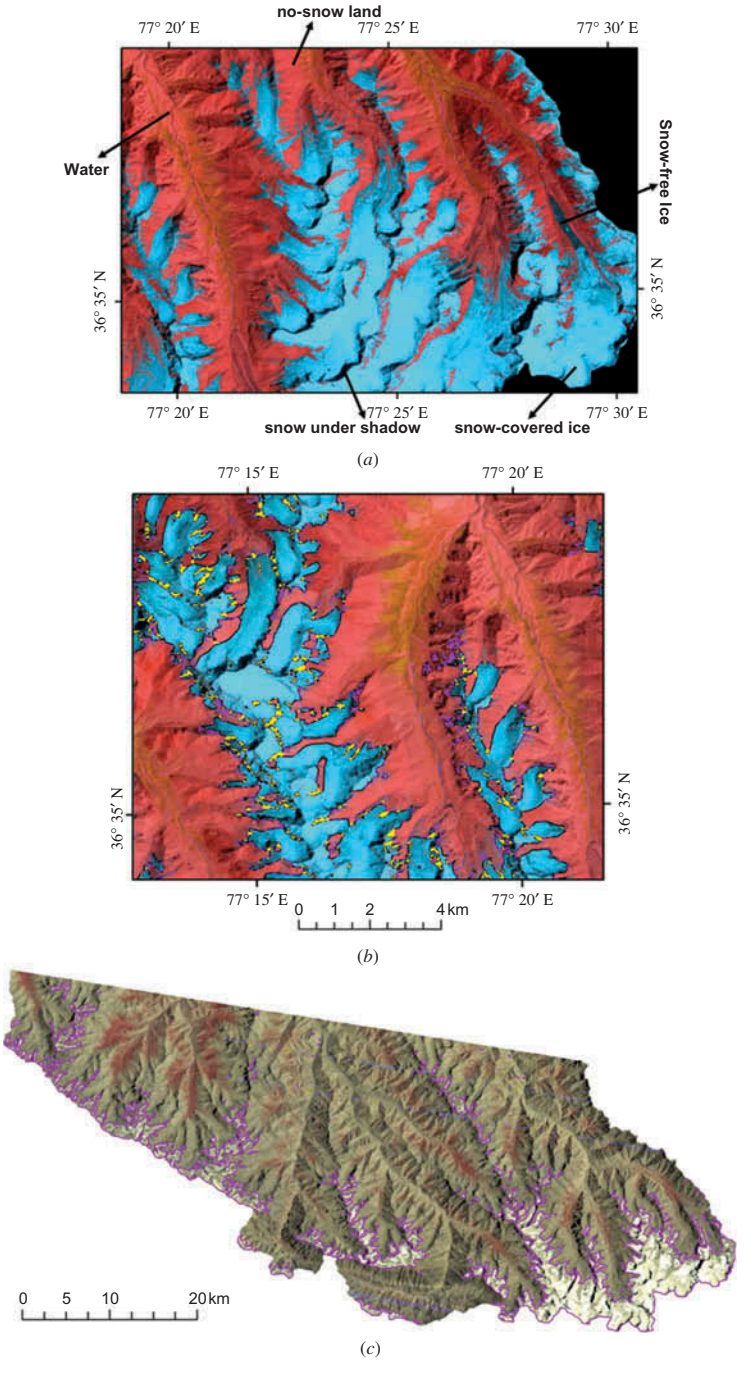

Figure 3. (*a*) Five training classes used in the supervised classification of snow cover from Landsat images in the southern portion of the Tizinafu watershed. (*b*) Detailed view of snow-cover classification results in the southern portion of the Tizinafu watershed. Black polygons denote the snow-cover intersection between the supervised classification and simple ratio of band4/band5. Purple and yellow indicate the areas unique to the supervised classification and band ratio methods, respectively. (*c*) Natural-colour Landsat MSS image of 14 July 1977 for the southern portion of the Tizinafu watershed in Figure 1(*a*) with snow cover (purple polygons) derived from the supervised classification method overlaid.

classification, these five classes were aggregated into two general classes: snow (snow under shadow, snow-covered ice, and snow-free ice) and no-snow (water and no-snow land). A detailed view of a portion of the snow cover extracted from the band ratio method and the supervised classification are shown in Figure 3(*b*). Since the training samples included snow under shadow, our supervised classification results were comparable to the band ratio result derived from the Landsat image. Figure 3(*c*) shows the snow cover extracted from the Landsat image of 14 July 1977 using the supervised classification method.

Seasonal snow and the limited availability of Landsat images made it impossible to study long-term glacier change within the watershed. Based on the comparability of spatial resolution and the amount and similarity of SCP, we used the Landsat images of 7 September 1998 and 10 August 2011 to study areal changes in three glaciers (D, E, F in Figure 1(*a*)). Following Paul et al. (2013), with some introduction and training, we asked 10 student analysts to manually digitize the glaciers from the two Landsat images.

3.3. *Corona image rectification and glacier digitization*

The cameras on the Corona missions were intended to produce panoramic stereo images for manual photograph interpretation. Since Corona images were collected with a panoramic camera, several types of geometric distortion are involved, and these distortions are maximized towards the edges of the photographs (Sohn, Kim, and Yom 2004). It is necessary to remove these distortions through rectification of Corona images. Corona camera model and sensor space positions are, however, difficult to obtain, and therefore, our Corona images had to be rectified by constructing empirical mathematic models through ground control points (GCPs) (Bolch, Pieczonka, and Benn 2011). ERDAS Leica Photogrammetry Suite™ (LPS; Leica Geosystems, Heerbrugg, Switzerland) photogrammetric software was used to rectify the subset (as indicated by the solid black rectangle in Figure 1(*a*)) of two Corona images. Our procedure first co-registered the Corona image to the Landsat ETM+ panchromatic imagery of 18 May 2001. This ETM+ image, downloaded from the Global Landcover Facility, was already orthorectified using a Shuttle Radar Topography Mission (SRTM) digital elevation model (DEM) (USGS 2009). The most difficult part was to find common points between the ETM+ panchromatic imagery and the Corona image because of the difference in snow condition, position of the sun, and spatial resolution. Stable river junctions and road intersections were used to collect 20 well-distributed GCPs (RMSE 2.01 m). Horizontal positions of the GCPs were acquired from the panchromatic imagery, and heights were derived from the SRTM DEM. ERDAS LPS created tie points (correlation threshold 0.65) and further improved the triangulation model for orthorectification.

Based on morphology and texture, three rock glaciers (A, B, and C in Figure 1(*c*)) were visually identified on both the orthorectified Corona image of 19 August 1968 and the Google Earth™ high-resolution image of 7 October 2007. Glacier boundaries on the Corona image were manually delineated using ESRI ArcScene™ software (ESRI, Redlands, CA, USA), where Corona images were draped on an Advanced Spaceborne Thermal Emission and Reflection Radiometer (ASTER) DEM of 30 m resolution to facilitate identification and digitization. The same glaciers were also digitized from Google Earth™ with its own 3D visualization and digitization capabilities. Manual delineation of glacier boundaries from the images, however, is subjective and may vary by operator. Following Paul et al. (2013), with some introduction and training, we asked 10 student analysts to digitize the glaciers and studied their boundary uncertainties.

4. Results

4.1. Snow-cover trends from 2002 to 2012

Compared with MODIS Terra (MOD10A1) and Aqua (MYD10A1) daily snow-cover data, the combination of Terra and Aqua data (MOYD10A1) reduced cloud obstruction by 2.4% and 5.8%, respectively. However, cloud is still a serious issue in MOYD10A1 data, where the mean number of days without clouds within a hydrological year is only 14.6. In three hydrological years (2008, 2010, and 2012) there were fewer than 10 cloud-free days, and there were no cloud-free days in the watershed between November and March from 2002 to 2012.

Using the most-recent-clear-observation de-cloud method, the daily cloud-cover percentage within the watershed was reduced to zero, a reduction of cloud cover of 40.9% on average. February and November had the largest and the least cloud-cover reduction (56.4% and 22.0%, respectively). This de-cloud method also increased daily SCP within the watershed by 3.0% on average. SCP had the largest increase of 7.4% in January, while in August it was reduced by 3.0%.

Annual and monthly mean SCPs and their standard deviations are shown in Figure 4. Mann–Kendall trend analysis indicated that there is no significant trend in annual mean SCPs ($p = 0.86$). Figure 4(*b*) shows the general pattern of SCP over 1 year. Snow typically starts melting from March until reducing to a minimum in August. From September, snow then begins accumulating until it reaches maximum the following February. There is a slight reduction in snow cover between October and December, which is probably because of snowmelt caused by direct solar irradiance and the lack of moisture in those months. Mann–Kendall trend analysis also indicated that no month had a significant trend in SCP.

The spatial distribution of SCF in each hydrological year is shown in Figure 5(*a*). Hydrological years 2007, 2009, and 2008 had the lowest annual mean SCF and also the lowest annual total stream flow at the watershed outlet, indicating snow as the main source of stream runoff. Hydrological years 2010, 2005, and 2006 had the highest annual mean SCF and the highest annual total stream flow at the watershed outlet. Mann–Kendall trend analysis indicated no trend in annual mean SCF ($p = 1$) over the 10 hydrological years.

Average and standard deviation of SCF for each cell during the 10 hydrological years are shown in Figures 5(*b*) and (*c*), respectively. Figure 5(*c*) shows that cells with either high or low SCF in the watershed had minimal inter-annual variation. The highest inter-annual variation in SCF occurred in the narrow bands next to the cells with the highest mean SCF (Figure 5(*b*)). Figure 5(*d*) shows SCF trends for each cell during the 10year period using Mann–Kendall trend analysis. The bands of cells with a high downward trend (negative slope and shaded blue in Figure 5(*d*)) are located between cells with the highest SCF (shaded red in Figure 5(*b*)) and those with a high upward trend (positive slope and shaded red in Figure 5(*d*)). However, only 0.66% of the cells exhibited significant downward or upward trends ($\alpha = 0.05$) and no spatial pattern was found for those cells.

AMSCPs (dotted line in Figure 6) were first calculated by finding the minimum daily SCP from June to September. They were also calculated by finding cells with SCF of 100% (dashed line in Figure 6). SCF-based AMSCPs are, except for the hydrological year of 2004, all lower than 1% and are on average 2% lower than AMSCPs derived from minimum daily SCP. This may be due to snow classification error caused by large sensor zenith angles of off-nadir MODIS scenes used to generate its snow-cover products (Dozier et al. 2008; Painter et al. 2012). Mann–Kendall analysis indicated that both AMSCPs have slight downward trends. However, neither downward trend was significant, with *p*-values of 0.86 and 0.24, respectively.

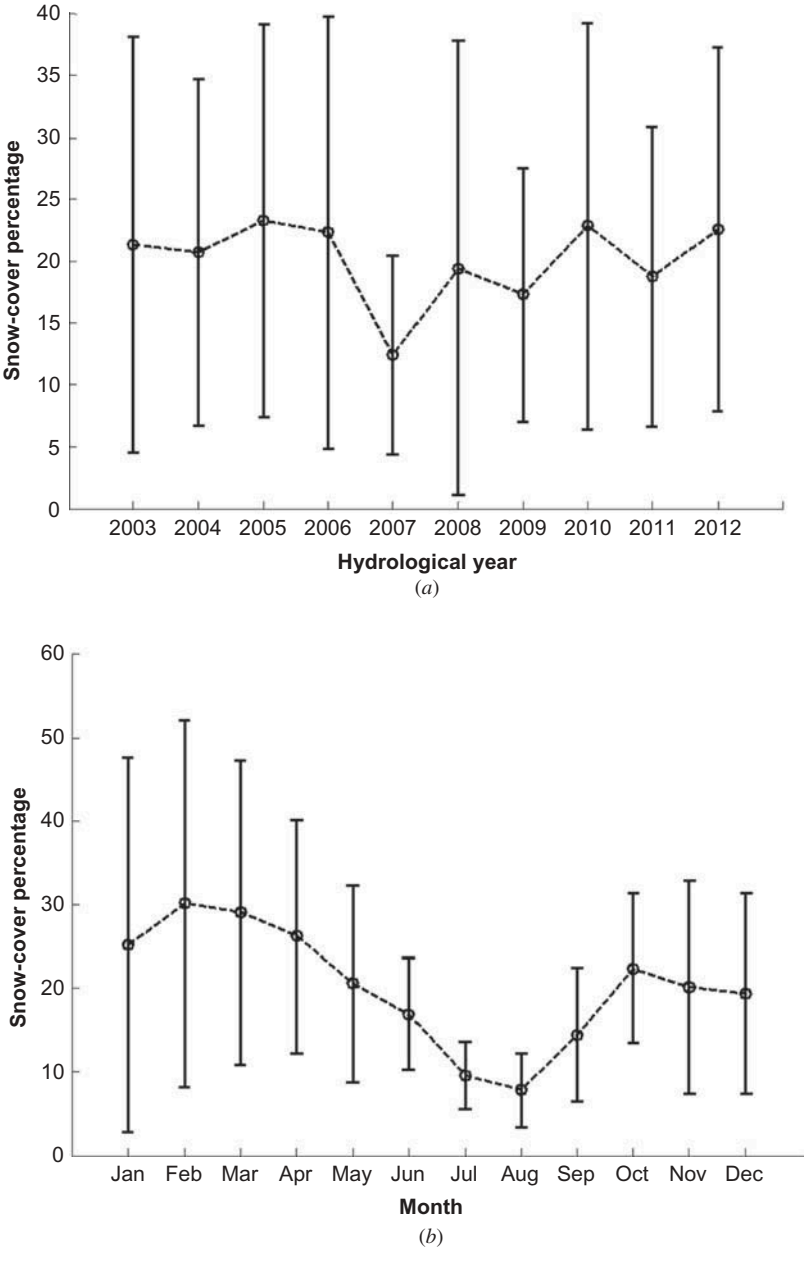

Figure 4. (*a*) Annual mean snow-cover percentage (SCP) of the Tizinafu watershed (Figure 1(*a*)) and standard deviation from 2003 to 2012; (*b*) monthly mean SCP in the watershed and standard deviation from 2003 to 2012.

4.2. Snow and glacier change from 1976 to 2011

We obtained and classified all 22 Landsat images available from 1976 to 2011 which had no cloud in the southern portion of the Tizinafu watershed (the area below the dotted black line in Figure 1). Those images are from June to September, when mean monthly

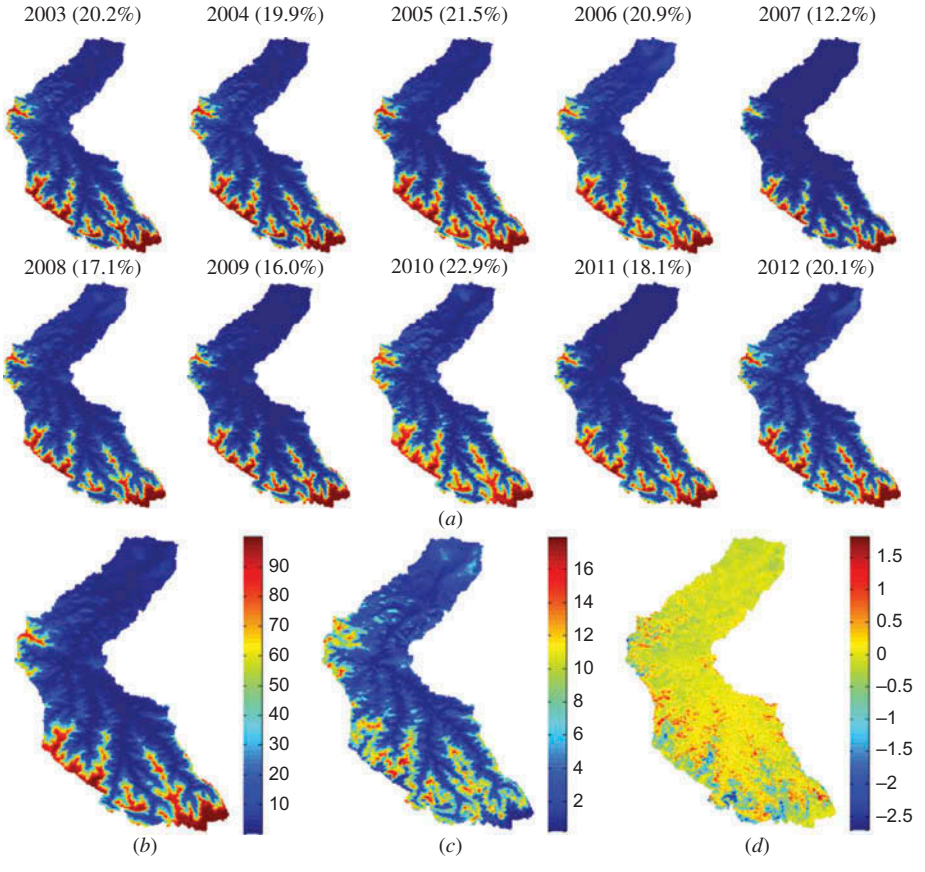

Figure 5. (*a*) Snow-cover frequency (SCF) in the Tizinafu watershed (Figure 1(*a*)) for each hydrological year from 1 October 2002 to 30 September 30 2012. SCF varies between 0 (blue) and 100 (red). Percentages in parentheses are mean SCFs of the watershed. (*b*) Mean hydrological-year SCF at each cell. (*c*) Standard deviation of hydrological-year SCF at each cell. (*d*) Downward (blue) or upward (red) trend of SCF at each cell over 10 hydrological years.

SCP in the watershed is lowest and has the least variation (see Figure 4(*b*)). Figure 7 shows the date, SCP, and spatial distribution of snow cover of each Landsat image within the watershed. Snow cover was classified using the band ratio method (band4/band5) for TM and ETM+ images and the supervised classification method for MSS images. SCPs vary from 13.2% to 65.7%, with a mean of 35.5% and standard deviation of 13.6%. Note that the Landsat SCPs are for the southern portion of the watershed and are much higher than MODIS SCPs of the entire watershed shown in Figure 4(*b*). It is clear from Figure 7 that there is seasonal snow in those months.

It's desirable also to examine the long-term trend of AMSCP using the available Landsat images from 1976 to 2011. However, the availability of Landsat images, their temporal resolution (~16 days), and frequent cloud obstruction in the watershed made it impossible to calculate AMSCP using Landsat images. Instead, we split the Landsat images into two groups, one with 11 images between 1976 and 2002 (Landsat1976 hereafter) and the other with 11 images from 2004 to 2011 (Landsat2004 hereafter). Table 1 lists the number of images and some SCP statistics in those groups. We tested the

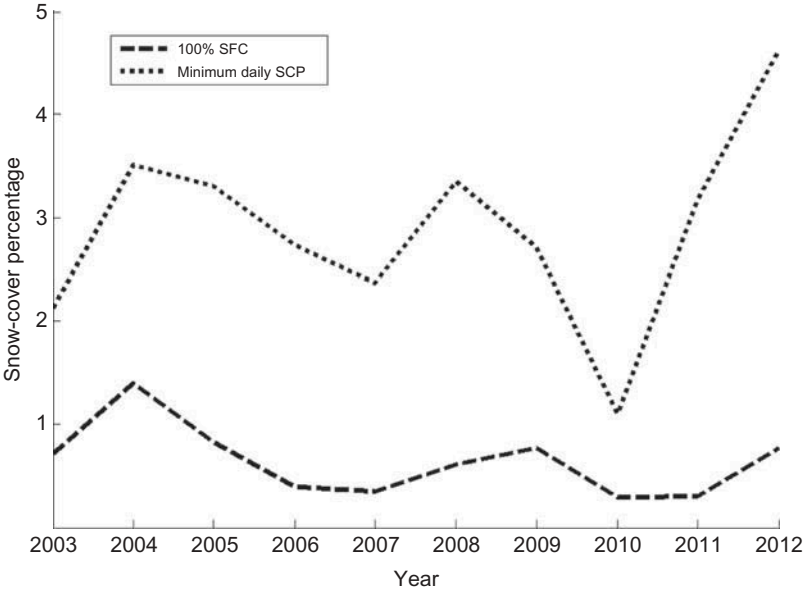

Figure 6. Annual minimum snow-cover percentage (AMSCP) for the Tizinafu watershed (Figure 1 (*a*)) calculated by finding the minimum daily snow-cover percentage (SCP) between June and September over 1 year (dotted line) and by using cells with a snow-cover frequency (SCF) of 100% (dashed line).

equality of variance and mean between the Landsat1976 and Landsat2004 groups; *p*-values for the variance and mean tests are 0.65 and 0.48, respectively, indicating no significant difference between the two groups in either variance or mean.

As confirmation of the Landsat images, we also calculated MODIS daily SCP on no-cloud days for the same months (June–August) within the southern portion of the watershed for the period 2003–2012 (MODIS2003 hereafter) to match the Landsat2004 group. The number of images and some SCP statistics for the group are also shown in Table 1. We tested the equality of variance and mean between Landsat2004 and MODIS2003 groups; *p*-values for the variance and mean tests for those two groups are 0.60 and 0.20, respectively, indicating no significant difference in either the variance or mean of SCP between the two groups. As those two groups cover roughly the same time period, this test provided confirmation that SCPs from Landsat images (a relatively small sample) and MODIS (a large sample) are comparable.

We also examined the uncertainty that might be caused by using slightly different band ratio threshold values. Here, we applied lower (1.5) and higher (2.5) thresholds to classify snow cover from 19 Landsat TM and ETM+ images. Each of the three Landsat MSS images was classified using three different sets of training sites. Using the lower threshold of 1.5, SCPs on the Landsat images are, by average, 2.8% higher than those using the threshold of 2.0. The minimum and maximum increase in SCP is 1.1% and 5.0%, respectively. Using the higher threshold of 2.5, SCPs are, on average, 2.3% less than those using the threshold of 2.0. The minimum and maximum decrease in SCP is 1.2% and 5.1%, respectively. We tested the equality of variance and mean between the Landsat1976 and Landsat2004 groups using the lower and higher thresholds. The *p*-values for the variance and the mean tests with the lower threshold are 0.74 and 0.49,

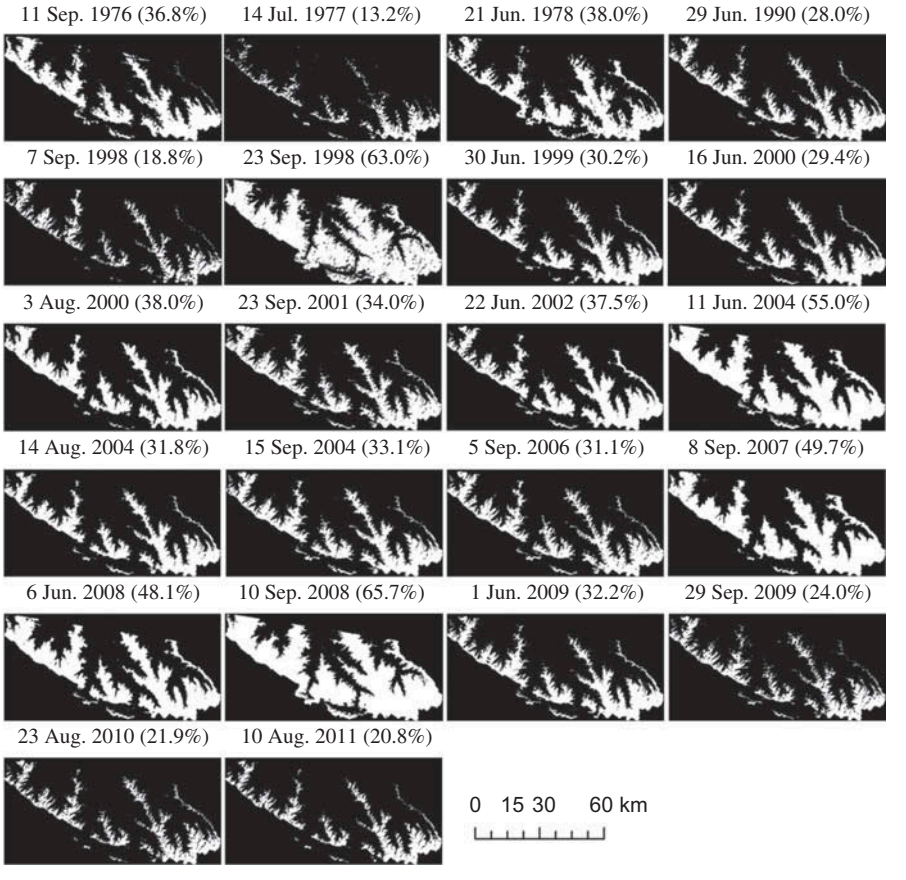

Figure 7. Landsat image date, snow-cover percentage, and snow cover (white) classified from 22 Landsat images from 1976 to 2011 for the southern portion of the Tizinafu watershed in Figure 1(*a*).

Table 1. Number of images and statistics of snow-cover percentage (SCP) for the three data groups.

Group (time period)	Number of images	Minimum SCP (%)	Maximum SCP (%)	Mean SCP (%)	SCP (%) variance
Landsat1976 (1976–2002)	11	13.2	63.0	33.4	162.8
Landsat2004 (2004–2011)	11	20.8	65.7	37.6	218.5
MODIS2003 (2003–2012)	95	9.5	78.1	32.0	181.8

respectively, and with the higher threshold are 0.56 and 0.43, respectively. Neither the lower nor the higher thresholds indicated significant difference in the variance or the mean of SCP between the two groups.

The three glaciers identified from the Landsat images of 7 September 1998 and 10 August 2011 and one digitization of their boundaries (D, E, and F in Figure 1(*a*)) are shown in Figure 8. The average areas for glaciers D, E, and F on the 1998 Landsat image

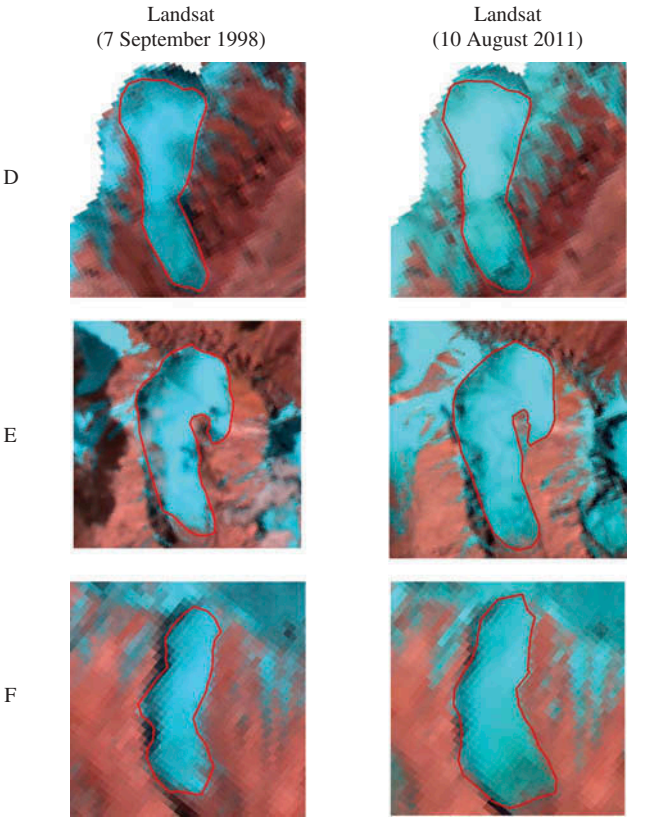

Figure 8. Three glaciers (D, E, and F in Figure 1(*a*)) identified on Landsat images of 7 September 1998 and 10 August 2011. One manual digitization of the boundaries (red) is overlaid on the images.

are 0.51, 1.45, and 0.18 km^2, respectively, and are 0.53, 1.62, and 0.26 km^2, respectively, on the 2011 Landsat image. The areas of glacier D, E, and F increased by 3.7%, 11.8%, and 44.1%, respectively. Overall, there is an areal increase of 12.6% for the three glaciers. The standard deviations of the digitized areas for glaciers D, E, and F are 3.2%, 3.4%, and 3.2% on the 1998 Landsat image, respectively, and 5.1%, 3.1%, and 7.3% on the 2011 Landsat image, respectively. Statistical tests of the equality of mean area between the two images yielded *p*-values of 0.07, 0.00, and 0.00, respectively, for glaciers D, E, and F. This indicated that there is no significant areal change in glacier D, but the increase in glaciers E and F is significant.

4.3. Glaciers changes between 1968 and 2007

A planar view of the three rock glaciers identified on the Corona image of 19 August 1968 and the Google Earth image of 7 October 2007, and one digitization of their boundaries, are shown in Figure 9. The average areas for glaciers A, B, and C are 0.98, 0.38, and 1.78 km^2 on the 1968 Corona image, respectively, and 0.94, 0.37, and 1.90 km^2 on the 2007 Google Earth image, respectively. While the average areas of rock glaciers A and B decreased by 3.6% and 1.8%, respectively, from 1968 to 2007, that of glacier C

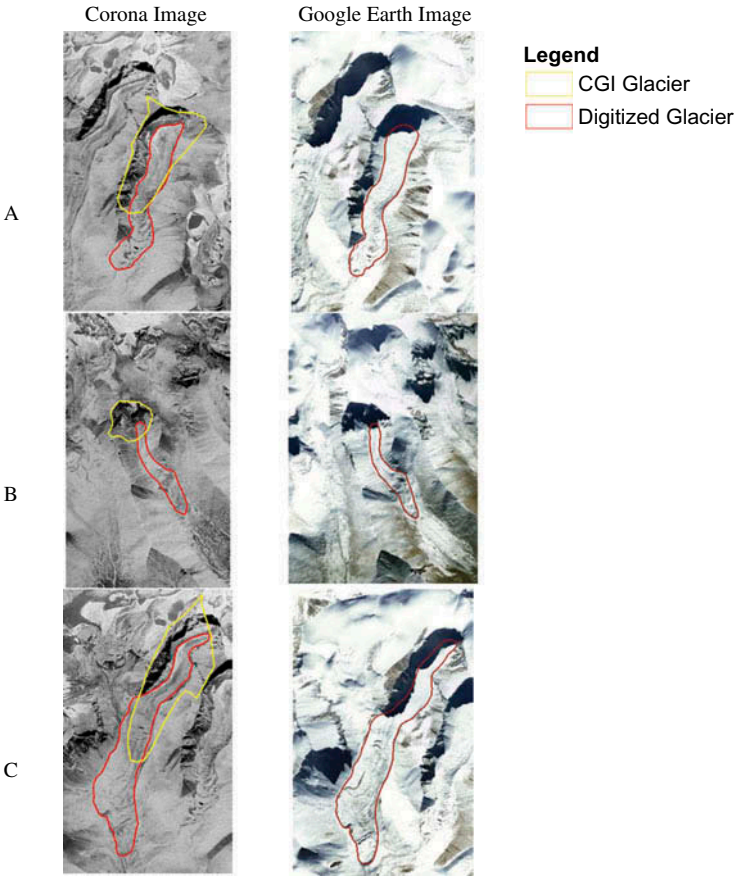

Figure 9. Planar view of the three rock glaciers (A, B, and C in Figure 1(*c*)) identified on the 1968 Corona image and the 2007 Google Earth image. One manual digitization of the glacier boundaries (red) and their boundaries from the Chinese Glacier Inventory (yellow) are overlaid on the images.

increased by 6.7% during the same period. Overall, the total area of the three rock glaciers increased by 2.5%. The standard deviations of the digitized areas for glaciers A, B, and C are 6.6%, 4.2%, and 4.2% on the Corona image, respectively, and 3.0%, 4.7%, and 4.7% on the Google Earth image, respectively. Statistical tests of the equality of mean area between the two images yielded *p*-values of 0.14, 0.36, and 0.00, respectively, for glaciers A, B, and C. This indicated that areal decrease in glaciers A and B is not statistically significant, but areal increase in glacier C is statistically significant.

5. Discussion

While remote sensing provides the primary (probably the only) data available for studying snow and glacier changes in remote mountain watersheds, our study revealed several limitations of those data sets. The first issue is the frequent cloud obstruction in mountain watersheds. With the MOYD10A1 data, which combined MODIS MOD10A1 (Terra) and MYD10A1 (Aqua) data, on average, only 14 days in 1 year are without cloud coverage. Further cloud reduction is necessary and can be achieved by using the land-cover type of

the last clear observation within a time window. We are currently developing a snow-frequency-based method of cloud reduction and are comparing the methods and the effects of the length of temporal window. AMSCP calculated from SCF revealed possible error in MODIS snow products caused by using off-nadir scenes with large sensor zenith angles. We will further investigate and compare our AMSCPs with the results from Painter et al. (2012).

Temporal resolution, availability of images, and cloud obstruction limit, if not prohibit, the use of Landsat images for long-term AMSCP trend analysis in mountain watersheds. This forced us to test only the equality of the variance and mean of SCPs over two time periods. Division of Landsat images into those two periods was also constrained by the uneven distribution of available images. Ideally, we would like to divide images into two equal periods. However, only one Landsat image (1990) was available for the 18 year period 1979–1997. Although we tested the equality of variance and mean of SCP between Landsat images and MODIS data for 2003–2012, we did not compare and assess snow-cover classification from those two remote-sensing platforms. We are currently evaluating the accuracy of snow-cover mapping products, especially for the snowmelt season, in the mountain watersheds of the Tarim River using a similar approach to that of Rittger, Painter, and Dozier (2012).

We initially aimed to study glacier change using Landsat images. However, seasonal snow and the limited availability of Landsat images made it impossible to study long-term change in individual glacier cover within the watershed. The 22 available Landsat images chosen were captured between June and September, during which the standard deviation of daily snow-coverage percentage is lowest (Figure 4(*b*)). Nevertheless, most of the Landsat images had seasonal snow (Figure 7) with SCP varying between 13.2% and 65.7%. Among the Landsat images, that of 7 September 1998 has the second lowest SCP and that of 10 August 2011 the third lowest. These two images also show the least difference in SCP among all pairs of images 10 or more years apart, with SCP less than 30%. Nonetheless, the SCP of the 2011 Landsat image is 2% higher than that of the 1998 image, and the extra seasonal snow is visible on the Landsat image of 2011 (Figure 8).

By comparing digitized glacier outlines from the CGI, which is based on data collected in the 1960s/1970s, and Landsat ETM+ images from 1999 to 2001, Shangguan (2009) investigated changes of 7665 (out of 11,665) glaciers in seven mountain watersheds (our watershed, unfortunately, is not one of these) in the Tarim River basin. Their results showed that total glacier area was reduced by 3.3% from the 1960s/1970s to 1999/2001, with a variation of 0.7% to 7.9% among watersheds. Neither the three real glaciers on the Landsat images nor the three rock glaciers on the Corona and Google Earth image in our study showed any significant reduction in extent. While the study of Shangguan (2009) is much more comprehensive than ours, their study also has potential limitations. The spatial resolution of the two data sources used in their study may not be compatible. CGI glaciers were mostly derived from aerial photographs and topographic maps from the 1960s and 1970s. Landsat images, however, have a much coarser resolution. In addition, it is still unclear how CGI glacier boundaries were delineated. Glacier boundaries delineated from the 1968 Corona image, which is similar to CGI data sources, are very different from their CGI boundaries (as shown in Figure 9). The quality of CGI data needs to be verified more extensively in the future.

Our analyses also have limitations. The glaciers identified from the Landsat images of 1998 and 2011 may not reveal any change because of the relatively short period involved (13 years). While the rock glacier images were captured 40 years apart, their reaction to climate change, however, is significantly slower than that of real glaciers (Haeberli et al.

2006; Berthling 2011). On the other hand, our results are consistent with Gardner et al. (2013). In their study, almost all sub-regions in the high-mountain Asia glaciers experienced negative elevation change except for the western Kunlun Mountains, which is where our study watershed is located. Shangguan (2009) also indicated in his study that the Hotian River, which is adjacent to our watershed, had the lowest rate of glacier reduction in the Kunlun Mountains.

6. Conclusions

Our study found no significant changes in snow and glaciers within the Tizinafu mountain watershed based on the analyses of 10 years' daily MODIS snow-cover data, 22 Landsat images from the 1970s, and high-resolution images from 1968 and 2007. Specifically, our study indicated no significant trend in either annual mean SCP or annual mean SCF during the 10 year period 2002–2012. Our analysis also showed no significant trend for mean SCP in any of the 12 months during the 10 year period. Spatially, the band of cells with high downward trend in SCF is located between cells with the highest SCF and the band of cells with high upward trend (Figure 5(*d*)). Again, only 0.66% of the cells showed a significant downward or upward trend.

Two approaches to calculating AMSCP were used and neither revealed any significant trend during the 10 year period. While it is impossible to study the long-term trend of AMSCP using the Landsat images available, our study found no significant difference in the variance and mean of SCP for two groups of Landsat images, one from 1976 to 2002 and the other from 2004 to 2012. Neither the glaciers from the Landsat images nor the rock glaciers from the Corona and Google Earth images indicated any significant reduction in extent. In summary, based on the analyses of multisource remote-sensing data sets, our study found no evidence of significant changes in snow and glacier cover in the Tizinafu mountain watershed.

Our results are different from Shangguan (2009), in which all the major glaciers in the mountain watersheds in the Tarim River basin showed significant area reduction. Although there are some data limitations in our study, our result is consistent with Gardner et al. (2013), which showed that almost all sub-regions in the high-mountain Asia glaciers experienced negative elevation change except for the western Kunlun Mountains, which is where our study watershed is located. Many previous studies on glacier changes in the region were based on CGI data whose quality, as shown in our study, needs to be further examined. Our future study will continue to resolve those issues and will expand our analyses to other mountain watersheds in the Tarim River basin.

Acknowledgements

This study is supported by the 'One Hundred Talents Programme' of the Chinese Academy of Sciences and the National Basic Research Programme of China (973 Programme, no. 2010CB951003). Constructive criticism and comments by Dr Timothy Warner (Editor) and two anonymous referees are greatly appreciated.

References

Andreassen, L. M., F. Paul, A. Kääb, and J. E. Hausberg. 2008. "Landsat-Derived Glacier Inventory for Jotunheimen, Norway, and Deduced Glacier Changes Since the 1930s." *The Cryosphere* 2: 131–145.

Berthling, I. 2011. "Beyond Confusion: Rock Glaciers as Cryo-Conditioned Landforms." *Geomorphology* 131: 98–106.

Bhambri, R., T. Bolch, and R. K. Chaujar. 2011. "Mapping of Hebris-Covered Glaciers in the Garhwal Himalayas Using ASTER DEMs and Thermal Data." *International Journal of Remote Sensing* 32: 8095–8119.

Bhambri, R., T. Bolch, R. K. Chaujar, and S. C. Kulshreshtha. 2011. "Glacier Changes in the Garhwal Himalaya India from 1968 to 2006 Based on Remote Sensing." *Journal of Glaciology* 57: 543–556.

Bolch, T., and U. Kamp. 2006. "Glacier Mapping in High Mountains Using DEMs, Landsat and ASTER Data." *Grazer Schriften Der Geographie Und Raumforschung* 41: 37–48.

Bolch, T., A. Kulkarni, A. Kaab, C. Huggel, F. Paul, J. G. Cogley, H. Frey, J. S. Kargel, K. Fujita, M. Scheel, S. Bajracharya, and M. Stoffel. 2012. "The State and Fate of Himalayan Glaciers." *Science* 336: 310–314.

Bolch, T., T. Pieczonka, and D. I. Benn. 2011. "Multi-Decadal Mass Loss of Glaciers in the Everest Area (Nepal Himalaya) Derived from Stereo Imagery." *The Cryosphere* 5: 349–358.

Dashora, A., B. Lohani, and J. N. Malik. 2007. "A Repository of Earth Resource Information – CORONA Satellite Programme." *Current Science* 92 (7): 926–932.

Dery, S. J., and D. B. Ross. 2007. "Recent Northern Hemisphere Snow Cover Extent Trends and Implications for the Snow-Albedo Feedback." *Geophysical Research Letters* 34: 1–6.

Dozier, J. 1989. "Spectral Signature of Alpine Snow Cover from the Landsat Thematic Mapper." *Remote Sensing of. Environment* 28: 9–22.

Dozier, J., T. H. Painter, K. Rittger, and J. E. Frew. 2008. "Time-Space Continuity of Daily Maps of Fractional Snow Cover and Albedo from MODIS." *Advances in Water Resources* 31: 1515–1526.

Flanner, M. G., K. M. Shell, M. Barlage, D. K. Perovich, and M. A. Tschudi. 2011. "Radiative Forcing and Albedo Feedback from the Northern Hemisphere Cryosphere Between 1979 and 2008." *Nature Geoscience* 4: 151–155.

Frey, H., F. Paul, and T. Strozzi. 2012. "Complication of a Glacier Inventory for the Western Himalayas from Satellite Data: Methods, Challenges, and Results." *Remote Sensing of Environment* 124: 832–843.

Gardner, A. S., G. Moholdt, J. G. Cogley, B. Wouters, A. A. Arendt, J. Wahr, E. Berthier, R. Hock, W. T. Pfeffer, G. Kaser, S. R. M. Ligtenberg, T. Bolch, M. J. Sharp, J. O. Hagen, M. R. van den Broeke, and F. Paul. 2013. "A Reconciled Estimate of Glacier Contributions to Sea Level Rise: 2003 to 2009." *Science* 340: 852–857.

Gheyle, W., J. Bourgeois, R. Goossens, and K. Jacobsen. 2011. "Scan Problems in Digital CORONA Satellite Images from USGS Archives." *Photogrammetric Engineering and Remote Sensing* 77 (12): 1257–1264.

Haeberli, W., B. Hallet, L. U. Arenson, R. Elconin, O. Humlum, A. Kääb, V. Kaufmann, B. Ladanyi, N. Matsuoka, S. Springman, and D. Vonder Mühll. 2006. "Permafrost Creep and Rock Glacier Dynamics." *Permafrost Periglac. Process* 17: 189–214.

Hall, D. K., J. L. Foster, D. L. Verbyla, A. G. Klein, and C. S. Benson. 1998. "Assessment of Snow-Cover Mapping Accuracy in a Variety of Vegetation-Cover Densities in Central Alaska." *Remote Sensing of Environment* 66: 129–137.

Hall, D. K., J. P. Ormsby, R. A. Bindschadler, and H. Siddalingaiah. 1987. "Characterization of Snow and Ice Reflectance Zones on Glaciers Using Landsat Thematic Mapper Data." *Annals of Glaciology* 9: 104–108.

Hall, D. K., G. A. Riggs, and V. V. Salomonson. 1995. "Development of Methods for Mapping Global Snow Cover Using Moderate Resolution Imaging Spectroradiometer Data." *Remote Sens. Environ* 54: 127–140.

Hall, D. K., G. A. Riggs, and V. V. Salomonson, 2001. "Algorithm Theoretical Basis Document (ATBD) for the MODIS Snow and Sea Ice-Mapping Algorithms, NASA Web Conference." National Aeronautics and Space Administration, Washington DC. Accessed June 10, 2013. http://modis.gsfc.nasa.gov/data/atbd/atbd_mod10.pdf

Helsel, D. R., and R. M. Hirsch. 2002. "Statistical Methods in Water Resources." In *Techniques of Water Resources Investigations, Book 4, Chapter A3,* 522 p. Reston, VA: U.S. Geological Survey.

Immerzeel, W. W., L. P. H. van Beek, and M. F. P. Bierkens. 2012. "Climate Change Will Affect the Asian Water Towers." *Science* 328: 1382–1385.

Kaser, G., M. Grosshauser, and B. Marzeion. 2010. "Contribution Potential of Glaciers to Water Availability in Different Climate Regimes." *Proceedings of the National Academy of Sciences USA* 107 (47): 20223–20227.

Li, X., and M. W. Williams. 2008. "Snowmelt Runoff Modeling in an Arid Mountain Watershed, Tarim Basin, China." *Hydrological Processes* 22 (19): 3931–3940.

MODIS. 2010. Accessed 28 December 2012. http://modis-snow-ice.gsfc.nasa.gov/sug_c5.pdf

Naz, B., L. Bowling, and M. Crawford. Forthcoming. "Spatial and Temporal Glacier Changes in the Central Karakoram Himalaya Derived from Landsat Satellite and Climate Data." *Journal of Glaciology.*

Ohmura, A. 2006. "Changes in Mountain Glaciers and Ice Caps During the 20th Century." *Annals of Glaciology* 43 (1): 361–368.

Painter, T. H., M. J. Brodzik, A. Racoviteanu, and R. Armstrong. 2012. "Automated Mapping of Earth's Annual Minimum Exposed Snow and Ice with MODIS." *Geophysical Research Letters* 39: L20501. doi:10.1029/2012GL053340.

Parajka, J., and G. Bloschl. 2008. "Spatio-Temporal Combination of MODIS Images – Potential for Snow Cover Mapping." *Water Resources Research* 44: W03406. doi:10.1029/2007WR006204.

Paul, F., N. Barrand, S. Baumann, E. Berthier, T. Bolch, K. A. Casey, H. Frey, S. P. Joshi, V. Konovalov, R. LeBris, N. Mölg, G. Nosenko, C. Nuth, A. Pope, A. Racoviteanu, P. Rastner, B. Raup, K. Scharrer, S. Steffen, and S. Winsvold. 2013. "On the Accuracy of Glacier Outlines Derived from Remote Sensing Data." *Annals of Glaciology* 54: 171–182.

Paul, F., C. Huggel, A. Kääb, T. Kellenberger, and M. Maisch. 2002. "Comparison of TM-Derived Glacier Areas with Higher Resolution Data Sets." *EARSeL eProceedings* 2: 15–21.

Rittger, K., T. H. Painter, and J. Dozier. 2012. "Assessment of Methods for Mapping Snow Cover from MODIS." *Advances in Water Resources* 35: 367–380.

Shangguan, D. H. 2009. "Glacier Changes During the Last Forty Years in the Tarim Interior River Basin, Northwest China." *Progress in Nature Science* 19 (6): 727–732.

Shangguan, D. H., S. Y. Liu, Y. J. Ding, L. F. Ding, L. B. Xiong, D. H. Cai, G. Li, A. X. Lu, S. Q. Zhang, and Y. Zhang. 2006. "Monitoring the Glacier Change in the Muztag Ata and Konggur Mountains, East Pamirs, Based on Chinese Glacier Inventory and Recent Satellite Imagery." *Annals of Glaciology* 43 (1): 79–85.

Shi, Y., C. Liu, and E. Kang. 2010. "The Glacier Inventory of China." *Annals of Glaciology* 50 (53): 1–4.

Sohn, H. G., G. H. Kim, and J. H. Yom. 2004. "Mathematical Modeling of Historical Reconnaissance Corona KH-4b Imagery." *The Photogrammetric Record* 19 (105): 51–66.

USGS. 2009. *Global Land Survey*, 2000, Landsat ETM +, 30m scene p148r035_7dp20010518. Sioux Falls, SD: United States Geological Survey.

Viviroli, D., H. H. Durr, B. Messerli, M. Meybeck, and R. Weingartner. 2007. "Mountains of the World, Water Towers for Humanity: Typology, Mapping, and Global Significance." *Water Resources Research* 43: W07447. doi:10.1029/2006WR005653.

Wang, X., and H. Xie. 2009. "New Methods for Studying the Spatiotemporal Variation of Snow Cover Based on Combination Products of MOIDS Terra and Aqua." *Journal of Hydrology* 371: 192–200. doi:10.1016/j.jhydrol.2009.03.028.

Williams, R. S., D. K. Hall, and C. S. Benson. 1991. "Analysis of Glacier Facies Using Satellite Techniques." *Journal of Glaciology* 37: 120–128.

Yao, T. D., Y. Q. Wang, S. Y. Liu, J. C. Pu, and Y. P. Shen. 2004. "Recent Glacial Retreat in High Asia in China and Its Impact on Water Resource in Northwest China." *Science in China Ser.D Earth Science* 47 (12): 1065–1075.

Ye, Q. H., S. C. Kang, F. Chen, and J. H. Wang. 2006. "Monitoring Glacier Variations on Geladandong Mountain, Central Tibetan Plateau, from 1969 to 2002 Using Remote-Sensing and GIS Technologies." *Journal of Glaciology* 52: 537–545.

Zemp, M., M. Hoelzle, and W. Haeberli. 2009. "Six Decades of Glacier Mass-Balance Observation: A Review of the Worldwide Monitoring Network." *Annals of Glaciology* 50: 101–111.